



Crystal Engineering in 3D: Converting Nanoscale Lamellar Manganese Oxide to Cubic Spinel while Affixed to a Carbon Architecture

Journal:	<i>CrystEngComm</i>
Manuscript ID	CE-ART-04-2016-000861.R1
Article Type:	Paper
Date Submitted by the Author:	24-May-2016
Complete List of Authors:	Donakowski, Martin ; Postdoctoral Associate of the National Research Council; US Naval Research Laboratory, Surface Chemistry Branch, Code 6171 Wallace, Jean Marie; U.S. Naval Research Laboratory, Surface Chemistry Branch, Code 6171; Nova Research Inc, Sassin, Megan; U.S. Naval Research Laboratory, Surface Chemistry Branch, Code 6171 Chapman, Karena; Argonne National Laboratory, X-ray Science Division, Advanced Photon Source Parker, Joseph; U.S. Naval Research Laboratory, Surface Chemistry Branch, Code 6171 Long, Jeffrey; U.S. Naval Research Laboratory, Surface Chemistry Branch, Code 6171 Rolison, Debra; U.S. Naval Research Laboratory, Surface Chemistry Branch



Crystal Engineering in 3D: Converting Nanoscale Lamellar Manganese Oxide to Cubic Spinel while Affixed to a Carbon Architecture[†]

Received 00th January 20xx,
Accepted 00th January 20xx

DOI: 10.1039/x0xx00000x

www.rsc.org/

Martin D. Donakowski,^{a,b} Jean M. Wallace,^{b,c} Megan B. Sassin,^b Karena W. Chapman,^d Joseph F. Parker,^b Jeffrey W. Long,^b and Debra R. Rolison^{b,*}

By applying differential pair distribution function (DPDF) analyses to the energy-storage relevant MnOx/carbon system—but in a 3D architectural rather than powder-composite configuration—we can remove contributions of the carbon nanofoam paper scaffold and quantify the multiphasic oxide speciation as the nanoscale, disordered MnOx grafted to the carbon walls (MnOx@CNF) structurally rearranges in situ from disordered birnessite AMnOx (A = Na⁺; Li⁺) to tetragonal Mn₂O₄ to spinel LiMn₂O₄. The first reaction step involves topotactic exchange of interlayer Na⁺ by Li⁺ in solution followed by thermal treatments to crystal engineer the ~10-nm-thick 2D layered oxide throughout the macroscale nanofoam paper into a cubic phase. The oxide remains affixed to the walls of the nanofoam throughout the phase transformations. The DPDF fits are improved by retention of one plane of birnessite-like oxide after conversion to spinel. We support the DPDF-derived assignments by X-ray photoelectron spectroscopy and Raman spectroscopy, the latter of which tracks how crystal engineering the oxide affects the disorder of the carbon substrate. We further benchmark MnOx@CNF with nonaqueous electrochemical measurements versus lithium as the oxide converts from X-ray-amorphous birnessite to interlayer-registered LiMnOx to spinel. The lamellar AMnOx displays pseudocapacitive electrochemical behavior, with a doubling of specific capacitance for the interlayer-registered LiMnOx, while the spinel LiMn₂O₄@CNF displays a faradaic electrochemical response characteristic of Li-ion insertion. Our results highlight the need for holistic understanding when crystal engineering an (atomistic) charge-storing phase within the (architectural) structure of practical electrodes.

1. Introduction

Crystal engineering is typically performed on single-phase materials, but offers benefits and challenges when applied to improve the performance of charge-storing oxides in composite electrode structures. We recently reported the synthesis of a monolithic, porous, crystal-engineered electrode comprising nanoscale LiMn₂O₄ coating a carbon nanofoam paper (LiMn₂O₄@CNF).¹ This device-ready electrode architecture achieved full theoretical capacity (148 mA h g⁻¹ at 2 mV s⁻¹) of the Mn³⁺/Mn⁴⁺ couple in aqueous electrolyte and exhibited appreciable capacity at rates that approach those more typically used with electrochemical capacitors. The oxide-modified 3D electrode architecture was created by

synthesis of a birnessite Na⁺-compensated MnOx@CNF,² topotactic exchange of Li⁺ in solution for interlayer Na⁺, and then crystal engineering the Li⁺-compensated MnOx birnessite by thermal processing in appropriate atmospheres (argon, then air) to form nanometric cubic LiMn₂O₄ spinel affixed to the carbon nanofoam walls. The CNF form factor projects the high-rate characteristics of thin-film batteries and capacitors into an electrode structure of macroscale dimensions with greater energy content. The evolving structure of the manganese oxide coating was tracked primarily by solid-state ⁷Li NMR and X-ray absorption analyses (XANES and EXAFS) with comparison to appropriate manganese oxide standards.

The process of nanostructuring electrode materials in 3D architectures for optimal surface area and charge-insertion capacity is paramount to advance electrochemical energy-storage (EES) technology.^{3,4,5,6,7} However, the nanoscopic/amorphous character of the carbon and often of the active charge-storing phase itself obscures structural characterization of the technologically relevant electrode structure because of overlapping signals in X-ray absorption and X-ray diffraction, broad Raman and FTIR signals, and difficulties in microscopically evaluating disordered/amorphous materials. Recent developments in total scattering analyses yield more detailed structural information for noncrystalline and nanocrystalline materials,^{8,9,10,11,12} including those that

^a Postdoctoral Associate of the National Research Council (NRC).

^b U. S. Naval Research Laboratory, Surface Chemistry Branch (Code 6170), Washington, D.C., 20375, USA.

^c Nova Research, Inc., 1900 Elkin Street, Alexandria, VA 22308, USA.

^d X-ray Science Division, Advanced Photon Source, Argonne National Laboratory, Argonne, IL 60439, USA.

* Corresponding author. E-mail: rolison@nrl.navy.mil.

[†] Electronic Supplementary Information (ESI) available: Details of Raman, powder X-ray diffraction (PXRD), differential pair distribution function (DPDF) fitting, Raman spectra and fits, PXRD patterns and fits, DPDF patterns and fits. See DOI: 10.1039/x0xx00000x

undergo conversion or insertion/intercalation reactions in battery systems.^{13,14,15,16} Total scattering analyses are able to separate contributions of disparate phases for quantification and atomistic modeling;^{14,17} this capability offers advantages in characterizing EES-relevant composites because functional electrodes are inherently inhomogeneous and require advanced techniques to extract structural information.^{18,19}

Pair distribution function studies have previously been applied to manganese oxides in biogenic^{20,21} and oxygen-evolution systems.^{22,23} These and other mineralogical studies have shown manganese oxides to exist in multiple phases such as layered birnessite and 3D extended solids such as rutile, bixbyite, pyrolusite, cryptomelane, and spinel. In-situ synchrotron X-ray experiments have tracked ion-insertion reactions into manganese oxide, e.g., the lithiation/delithiation of $\text{LiNi}_0.4\text{Mn}_0.6\text{O}_x$, which follows a two-step mechanism in nonaqueous electrolyte.^{24,25} An ex-situ synchrotron XAS study of Na^+ -compensated birnessite MnO_x @CNF cycled in aqueous, concentrated Li/KOH electrolyte found an oxide structure-invariant mechanism in the pseudocapacitive potential window but a reversible structural interconversion when cycled in the battery (faradaic) region.²⁶

Tracking the structure of nanoscale materials via synchrotron XAS is less straightforward than pursuing a total scattering analysis. The frequency domain (k space) range of XAS data only provides sufficiently high-quality information for first- and second-shell interactions, which allows element-specific, but range-limited atomistic modeling of disordered/multiphase nanomaterials. This XAS limitation is particularly problematic for manganese oxides thanks to their noted polymorphic character. Because total scattering data provide real space atom-atom interactions that can extend up to tens of nanometers as well as the intensity, width, and positional energy of all peaks, any structural differences between multiple phases within a material are more readily modelled.

Herein, we analyze a synthetically nanostructured 3D Na^+ -compensated birnessite MnO_x -painted carbon nanofoam paper as the oxide undergoes phase transformation via topotactic ion exchange, improved ordering of the birnessite MnO_6 layers by incorporation of interlayer Li^+ , and phase conversion to primarily 3D lithiated spinel. Notably, during the crystal engineering process, the manganese oxide-modified 3D electrode converts from an electrochemical pseudocapacitor birnessite phase NaMnO_x @CNF to a nanocrystalline $\text{Mn}_3\text{O}_4/\text{LiMn}_2\text{O}_4$ @CNF composite exhibiting battery-like charge storage. The use of total scattering techniques to examine composite materials allows structural determination and correspondingly, structure-property correlation to explain complex composite electrochemical energy-storage behaviors.

2. Experimental Methods

2.1 Materials

Argon gas (Earlbeck Gases & Technologies); resorcinol (99%; Sigma-Aldrich), formaldehyde (36.5–38% in water with 10–15% methanol as stabilizer, Sigma-Aldrich); sodium

permanganate monohydrate (97+%; Sigma-Aldrich), sodium sulfate (99+%; Strem), sodium carbonate (A.C.S. certified; MCB), 1 M LiPF_6 in a 1:1:1 mixture of ethylene carbonate: diethyl carbonate:dimethyl carbonate (EC/DC/DMC; BASF), lithium nitrate (99%; Alfa-Aesar), and aluminium foil (0.13-mm thick, 99.9995% metals basis; Alfa-Aesar) were used as received. Water for all procedures was 18 M Ω cm (ThermoScientific). Immediately before use for synthesis of CNFs, the carbon fiber paper (density 0.2 g cm⁻³, 90- μm thick; Lydall) was etched for 30 min in an RF glow-discharge plasma reactor (Harrick) in ambient air with ice chips added to the chamber. Nanoparticulate LiMn_2O_4 (Altair Nano) and crystalline Mn_3O_4 (Sigma, 97%) were used as standards for Raman spectroscopy and DPDF analysis.

2.2 Syntheses of MnO_x @CNF Composites

We synthesized carbon nanofoams (CNFs) as previously described^{27,28} to obtain a pore distribution characteristic of nanofoam papers prepared using 50 wt% resorcinol/formaldehyde and a 1500:1 resorcinol-to-catalyst ratio (see Supporting Information, Fig. S1[†])

Caution: formaldehyde has been classified as a carcinogen, so personal protection equipment must be used; minimizing inhalation exposure is advised.

The process flow used to synthesize and modify/topotactically engineer the manganese oxide/nanofoam composite is shown in Fig. 1. The sodium

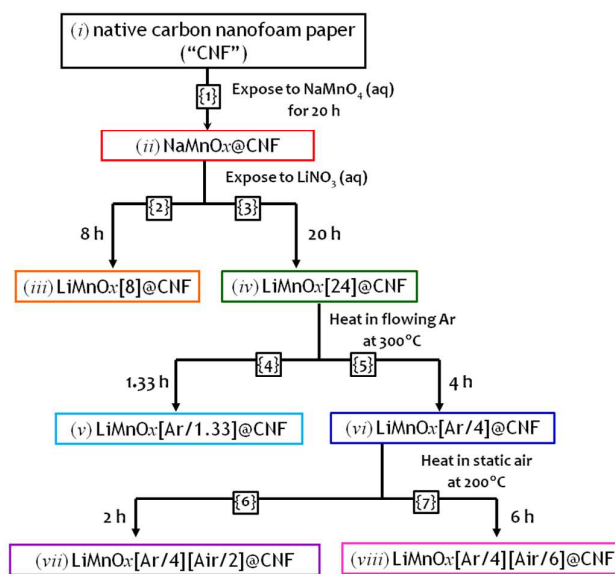


Fig. 1 The synthesis of MnO_x composites from CNF. Process {1} treats CNF (i) with an aqueous solution of $\text{NaMnO}_4 \cdot \text{H}_2\text{O}$ to generate NaMnO_x @CNF (ii); process {2} soaks (ii) in aqueous 1 M $\text{LiNO}_3 \cdot \text{H}_2\text{O}$ for 8 h to exchange Na^+ for Li^+ to create LiMnO_x [8]@CNF while process {3} equilibrates (ii) with aqueous 1 M $\text{LiNO}_3 \cdot \text{H}_2\text{O}$ for 24 h to create LiMnO_x [24]@CNF (iv). Process {4} heats (iv) in flowing argon at 300°C for 1.33 h to generate LiMnO_x [Ar/1.33]@CNF (v), and process {5} heats (iv) in argon at 300°C for 4 h to generate LiMnO_x [Ar/4]@CNF, (vi). Process {6} heats (vi) in static air at 200°C for 2 h to create LiMnO_x [Ar/4][Air/2]@CNF, (vii) while process {7} heats (vi) in static air at 200°C for 6 h to generate LiMnO_x [Ar/4][Air/6]@CNF, (viii).

manganese oxide-coated CNF (NaMnO_x@CNF), composite (ii), is processed in a manner as described by Fischer et al. and Sassin et al.^{1,2} Ion exchange was commenced by infiltrating multiple pieces of NaMnO_x@CNF with aqueous 1 M LiNO₃•H₂O. After 8 h, pieces of LiMnO_x[8]@CNF, composite (iii), were removed and copiously rinsed with water and vacuum infiltrated with water for 1 h (repeated three times). The remaining NaMnO_x@CNFs were vacuum infiltrated with 1 M aqueous LiNO₃•H₂O for an additional 16 h and then rinsed with copious amounts of water to create LiMnO_x[24]@CNFs, composite (iv). Composites (iii) and (iv) were dried under flowing N₂ at 45 °C for 24 h.

Samples of LiMnO_x[24]@CNF were then placed in a furnace under flowing argon and heated at a rate of 2 °C min⁻¹ to 300 °C, held for 1.33 h, and then cooled at 2 °C min⁻¹ to ambient to generate LiMnO_x[Ar/1.33]@CNF, composite (v). Samples of LiMnO_x[24]@CNF were also heated in argon at 2 °C min⁻¹ to 300 °C, held for 4 h, then cooled at 2 °C min⁻¹ to ambient conditions to generate LiMnO_x[Ar/4]@CNFs, composite (vi). Samples of LiMnO_x[Ar/4]@CNF were rapidly heated in static air by directly introducing the samples into a furnace held at 200 °C, then removing the samples after either 2 h or 6 h to respectively generate LiMnO_x[Ar/4][Air/2], composite (vii), or LiMnO_x[Ar/4][Air/6], composite (viii).

Control samples for Raman spectroscopy were produced by omitting deposition of manganese oxide. Bare CNFs were immersed in 1 M LiNO₃•H₂O for 24 h, copiously rinsed, then dried in a flow of N₂ at 45 °C for 24 h; a Li⁺-soaked CNF was set aside. The remaining CNFs were heated in argon at 2 °C min⁻¹ to 300 °C, held for 4 h, then cooled at 2 °C min⁻¹ with a Li⁺-soaked, Ar-heated CNF set aside. A Li⁺-soaked, Ar-heated CNF was heated in static air by placing it in a preheated oven for 6 h and immediately removing the CNF to obtain a Li⁺-soaked, Ar-heated, and air-heated CNF control.

2.3 Characterization of AMnO_x@CNF composites.

2.3.1 Powder X-ray diffraction (PXRD)

Laboratory powder X-ray diffraction data were collected on a Rigaku SmartLab X-ray diffractometer at a fixed Cu K α radiation ($\lambda = 1.5406 \text{ \AA}$). The scans were recorded from $2\theta = 10$ to 60° , with a 0.02° step size and an integration time of 1 s per step; the PXRD data are shown in Fig. 2. The synchrotron PXRD data were obtained on LiMnO_x@CNF[Ar/4][Air/6], composite (viii), at 11-BM of the Advanced Photon Source (APS) at Argonne National Laboratory via the mail-in program with a 1-h acquisition over $2\theta = 0.5\text{--}50^\circ$, $\lambda = 0.414208 \text{ \AA}$. The data were fit via the Rietveld method in GSAS-II.²⁹

2.3.2 Differential Pair Distribution Function (DPDF)

To analyze the amorphous/nanoscale oxide content of the various MnO_x@CNFs, we performed differential pair distribution function (DPDF) analyses.^{11,30,31} The MnO_x@CNF composites were mechanically exfoliated with a mortar and pestle and the resulting powders were placed into Kapton capillaries (1.02-mm inner diameter; MicroLumen). Standards for comparison were made by combining mechanically exfoliated CNF with LiMn₂O₄ and mechanically exfoliated CNF with Mn₃O₄ (50:50 ratio by weight). Pair distribution function

(PDF) data were acquired on 11-ID-B (APS) using the rapid-acquisition pair distribution function (RA-PDF) technique with a Perkin-Elmer α -Si detector,⁸ $\sim 58 \text{ keV}$ X-ray radiation ($\lambda = 0.2114 \text{ \AA}$), and a sample-to-detector distance of 17.3 mm. We collected total scattering data with 360 frames of 0.5-s exposures for optimal counting statistics, integrated the data in Fit2D,³² numerically subtracted the signal from a Kapton blank, and processed the data from $Q_{\text{min}} = 0.0 \text{ \AA}^{-1}$ to $Q_{\text{max}} = 24.1 \text{ \AA}^{-1}$ in PDFGetX3 with a blank CNF as the null sample to account for contributions from the CNF substrate.³³ The CNF scaling factor was optimized in PDFGetX3 to eliminate the feature at $\sim 1.4 \text{ \AA}$ associated with the carbon-carbon bond, because the manganese oxide materials studied cannot have radial correlations below $\sim 1.9 \text{ \AA}$.

The acquired DPDF data were fit in PDFGui with structural models of various manganese oxides, including the expected ion-compensated birnessites and spinel.³⁴ Instrumental broadening contributions as denoted by the values for Q_{damp} (0.0400) and Q_{broad} (0.0178) were obtained from an external standard of nickel powder. We performed fits over the range $0.8\text{--}30 \text{ \AA}$ for all MnO_x@CNF variants by considering single and multiphase models and using isotropic displacement factors to refine the final fit. Fits of the birnessite AMnO_x materials included a term that uniformly increases the isotropic parameters of all atoms along the *c* axis to model turbostratic disorder of the MnO₆ sheets. The particle size of the oxide was fixed at 4 nm to account for correlations observed between 20–30 \AA .

Fits of the DPDF data for the thermally processed composites were performed by fitting the nanocrystalline components LiMn₂O₄ and Mn₃O₄ over the range $0.8\text{--}30 \text{ \AA}$ with sequential refinements between LiMn₂O₄ and Mn₃O₄ of cell parameters and scale factor, isotropic atomic displacement, and long-range broadening parameters between each. For argon-heated (v) and (vi) the size of Mn₃O₄ and LiMn₂O₄ were fixed at 10 nm based upon estimates obtained from Rietveld analysis. Heat treatment in air caused an apparent particle size decrease in the DPDF patterns and the particle size of Mn₃O₄ and LiMn₂O₄ were refined for the DPDF patterns of (vii) and (viii). Detailed fits, including the residuals between observed and fit patterns, are provided in Supporting Information (Figs. S24–S33[†]).

2.3.3 Raman Spectroscopy

We collected Raman spectra of (i)–(viii) with a Renishaw inVia Raman microscope equipped with an argon ion laser (514 nm) source accumulating 0.5-s scans at 0.135 W for an average of 1024 scans for each sample. The various MnO_x@CNF papers were placed on a stage and the microscope was focused with a 50 \times aperture on the surface of the MnO_x@CNF to maximize signal from the nanofoam over that from the carbon fiber-supporting struts. Scans were additionally obtained for nanoparticulate LiMn₂O₄ and crystalline Mn₃O₄. See supporting information for spectra and the fits to bands of graphitic carbon stretches (Figs. S2–S11[†]).

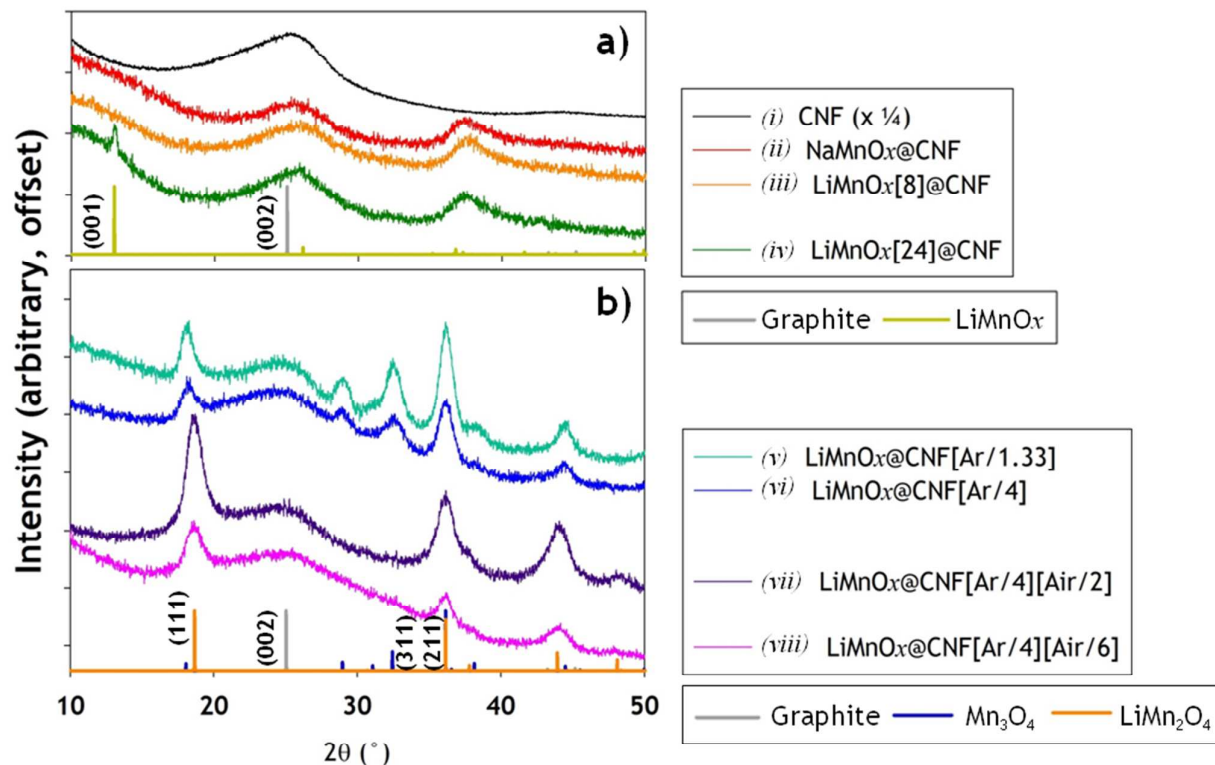


Fig. 2 Powder X-ray diffraction (PXRD) patterns taken with laboratory Cu K α radiation ($\lambda = 1.54056 \text{ \AA}$) of **a)** CNF (i) at 25% intensity and the unheated composites AMnO $_x$ (ii)–(iv); Miller indices of major peaks for the lamellar AMnO $_2$ phase are noted. The decrease in intensity of the AMnO $_x$ @CNF composites relative to the CNF is due to X-ray absorption by the AMnO $_x$ phase(s). The peak exhibited at $\sim 13^\circ 2\theta$ for LiMnO $_x$ [24] arises from lamellar coherence of birnessite MnO $_x$ upon lithium exchange. **b)** composites (v)–(viii) were heated in flowing argon and static air for as-noted durations. The identity/quantity of tetragonal A'Mn $_2$ O $_4$ and LiMnO $_x$ varies. For all PXRD patterns, the data quality is degraded because of the nanoscopic/amorphous character of the MnO $_x$ and CNF phases. Note that the (311) index of cubic spinel LiMn $_2$ O $_4$ overlaps with the (211) index of tetragonal Mn $_3$ O $_4$.

2.3.4 X-Ray Photoelectron Spectroscopy (XPS)

The relative concentrations of C, Mn, and Na were determined by X-Ray photoelectron spectroscopy (XPS) using a Thermo Scientific K-Alpha X-ray photoelectron spectrometer at a chamber pressure $< 5.0 \times 10^{-8}$ Torr and equipped with a monochromatic Al K α source (1486.68 eV) using a 400- μm elliptical spot size. The spectra were analyzed with Avantage[®] software version 5.35. The atomic percent of Li was not ascertained by XPS because of strong overlap of the Mn 3p peak and the low Scofield sensitivity factor of Li 1s.

2.3.5 Scanning Electron Microscopy

To evaluate oxide morphology and surface roughness we performed scanning electron microscopy (SEM). Micrographs were obtained on a Leo Supra 55 SEM at an accelerating voltage of 10 keV. Samples were adhered to stubs with conductive carbon tape (Ted Pella).

2.3.6 Electrochemical Analysis

Cyclic voltammetry (CV) was run in an electrolyte of 1 M LiPF $_6$ in ethylene carbonate/diethyl carbonate/dimethyl carbonate (EC-DC-DMC) with lithium metal foil as counter electrode, a separate lithium metal foil as reference electrode,

and as the working electrode, a $0.5 \times 0.5 \text{ cm}^2$ square of MnO $_x$ @CNF glued to an aluminium current collector with carbon paste (Electrodag EB-012; Acheson). Voltammetric scans were performed at 0.5 mV s^{-1} between 3.0–4.4 V vs. Li. The pseudocapacitive and Faradaic charge storage was determined by integration between 3.05–4.35 V vs. Li in Gamry Echem Analyst V5.58 and normalized to the total mass of the oxide@CNF composite electrode (coulombs per gram electrode).

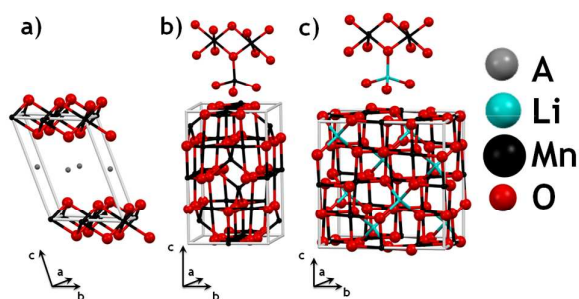


Fig. 3 a) The structure of the birnessite AMnO_x phase with lamellar MnO_6 layers separated by alkali metal ions ($\text{A} = \text{Na}^+, \text{Li}^+$). b) A fragment and unit cell of the tetragonal Mn_3O_4 phase. c) A fragment and unit cell of the cubic spinel LiMn_2O_4 phase. Although the local structure of LiMn_2O_4 and Mn_3O_4 are similar, the scattering intensities of tetrahedral Li and Mn vary greatly and the extended structures of the cubic and tetragonal phases differ slightly.

3. Results and Discussion

3.1 Analysis of structure by powder X-ray diffraction

Conventional materials characterization techniques were first employed to examine the electrodes. Powder X-ray diffraction (PXRD) data show broad reflections from the supporting carbon, which conceal peaks of other phases (Fig. 2). Rietveld fits of the diffraction data were based on modeling the carbon as graphitic with contributions from the oxide phases shown in Fig. 3; the lamellar birnessite AMnO_2 phase ($\text{A} = \text{Na}^+, \text{Li}^+$) contains infinite sheets of MnO_6 octahedra along the ab plane (Fig. 3a). Birnessite AMnO_2 is described by a monoclinic spacegroup $C2/m$ with Mn on the corners of the unit cell and center of the ab faces of the unit cell. The MnO_6 slabs are separated by alkali cations A^+ located on the ac and bc faces unit cell and are coordinated by an indeterminate number of water molecules. The hausmannite Mn_3O_4 phase is a tetragonal spinel of spacegroup $I4_1/amd$ with $\text{Mn}^{2+/3+}$ cations located on both the tetrahedral and octahedral sites (Fig. 3b). The cubic LiMn_2O_4 phase is described by the $Fm\bar{3}m$ spacegroup and has Li^+ ions on the tetrahedral sites and $\text{Mn}^{2+/3+}$ ions on the octahedral sites (Fig. 3c). The fit parameters of the individual PXRD patterns are supplied in the supporting information (Tables S4–S12[†]). Coating the CNF with MnO_x decreases the raw scattering intensity by $\sim 75\%$ relative to the unmodified CNF. The intensity decrease arises because X-rays penetrating into the porous, but macroscale-thick nanofoam paper intersect tens or more randomly oriented MnO_x ||C interfaces, which have a higher X-ray absorption coefficient relative to carbon-only interfaces. All of the composites show diffuse scattering associated with nanoscopic carbon, which fits to a coherent graphene crystallite size of approximately 1 nm.

For the ion-compensated lamellar MnO_x series, composites (ii)–(iv), the increased scattering present at $2\theta \sim 38^\circ$ cannot be adequately fit with a model of only graphitic carbon and may arise from disordered carbon and the presence of disordered MnO_x phases. The (00l) characteristic reflections of birnessite AMnO_x , visible but broadened for nanoscopic birnessite of comparable characteristic dimensions,³⁵ should appear over a 2θ range of $20\text{--}70^\circ$, but are obscured for all AMnO_x @CNF variants. The absence of birnessite peaks for AMnO_x is attributed to the large scattering contribution of the disordered, nanoscopic carbon of the CNF.

Composite (iv), LiMnO_x [24], the end point for the Na^+/Li^+ topotactic exchange, shows a peak at $\sim 13^\circ 2\theta$ (Fig. 2a) that can only be fit to a (001) Bragg reflection off a 6.75 \AA interlayer spacing between MnO_6 sheets of the birnessite structure (Fig. 3a). This sharp, low 2θ peak is not present for composites (ii) and (iii), the CNFs coated respectively with Na^+ -only compensated birnessite or LiMnO_x [8] birnessite. The XPS analyses show that LiMnO_x [8] and LiMnO_x [24] have Na^+ essentially fully replaced by Li^+ (Fig. S12[†]). Alignment of the MnO_6 sheets is neither driven by merely replacing interlayer Na^+ with Li^+ nor by a long soak in a concentrated salt solution. Immersing NaMnO_x @CNF in aqueous 1 M NaNO_3 for 24 h does not create a nanofoam-supported oxide with a (001) lamellar reflection (see Fig. S22[†]). Taken together, we posit that hydrated Li^+ (in solution, $\sim 600 \text{ pm}$ in size with >10 waters of hydration) serves as the interlayer lubricant by which the turbostratic disorder of the MnO_6 sheets is lessened over 24 h to exhibit lamellar registry.

After heating LiMnO_x [24]@CNF in argon at 300°C , the Rietveld refinements for composites (v) and (vi), LiMnO_x [Ar/1.33]@CNF and LiMnO_x [Ar/4]@CNF, respectively, show that the birnessite phase converts to 3D extended phases with coherent crystallite sizes of $\sim 10 \text{ nm}$ —primarily

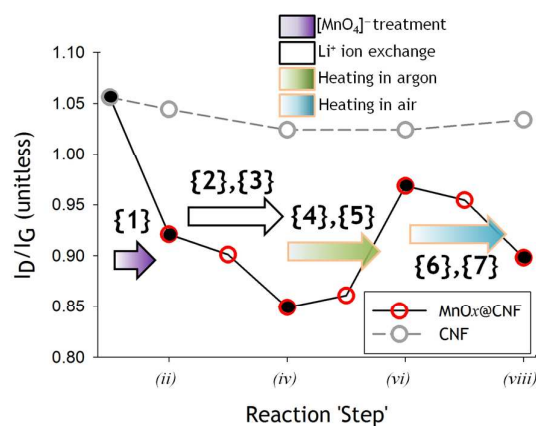


Fig. 4 The ratio of intensity of the D band to G band of the Raman spectra of CNF composites as a function of reaction sequence: the x axis refers to composites (i)–(viii) depicted in the synthesis scheme of Fig. 1. The filled red circles refer, respectively, to (i) CNF, (ii) NaMnO_x @CNF, (iv) LiMnO_x [24]@CNF, (vi) LiMnO_x [Ar/4]@CNF, and (viii) LiMnO_x [Ar/4][Air/6]@CNF. The gray, dotted line indicates control CNF samples that were processed through the reaction sequence without a MnO_x coating.

comprising tetragonal Mn_3O_4 (hausmannite) plus a small amount of defective cubic LiMn_2O_4 . Subsequent heating in static air of $\text{LiMnO}_x[\text{Ar}/4]@\text{CNF}$ to composites (vii) and (viii) converts the CNF-affixed oxide to cubic LiMn_2O_4 with a trace of Mn_3O_4 . The reflections for cubic/tetragonal $\text{A}'\text{Mn}_2\text{O}_4$ ($\text{A}' = \text{Li}^+$, Mn^{2+}) are difficult to deconvolve with traditional X-ray (Rietveld) methods—particularly in the presence of a large contribution of diffuse scattering to the PXRD pattern from the pyrolytic carbon comprising the CNF.

The Rietveld refinements of the PXRD patterns for all of the composites do not, however, provide quantification of either multiple phases or the degree of order/disorder present in the oxide coatings because of the nanoscopic, disordered, and composite nature of these MnO_x -modified CNFs. The most PXRD-crystalline specimen, composite (viii), in which the oxide is predominantly cubic LiMn_2O_4 spinel, was examined using synchrotron XRD (Fig. S21[†]). Although the higher fluence and resolution inherent to this instrument frequently improves analysis of nanoscopic materials, the resulting pattern for this composite contains broad, overlapping Bragg peaks, again thwarting quantitative Rietveld refinement.

3.2 Effect on the carbon substrate of crystal engineering birnessite to spinel: Analysis of order/disorder by Raman spectroscopy

Raman spectroscopy effectively probes relative order and disorder of carbonaceous materials as a function of the intensity of the disordered (I_D) and graphitic (I_G) bands.^{36,37} For amorphous carbon, I_D and I_G are defined by the height of the peaks.³⁶ The D peak arises from breathing modes of six-atom rings that contain a defect; the G peak occurs owing to the E_{2g} phonon. Relative to bulk carbon, nanoparticulate carbon inherently exhibits greater $\text{sp}^3:\text{sp}^2$ ratios because of an increased number of edge defects. Fits of the Raman spectra to Lorentzian functions for the unmodified CNF and all $\text{MnO}_x@\text{CNF}$ composites (see Figs. S3–S10[†]) provide the I_D and I_G values (Fig. 4) through the entire processing sequence described in Fig. 1. A Gaussian located at 1195 cm^{-1} , which is attributed to point defects (missing carbon atoms) in a tetrahedral network, also seen for carbon blacks and defective diamond-like carbon, is present in the Raman spectrum of the unmodified CNF (Fig. S2[†] and Fig. S3[†]) and absent after MnO_x functionalization.³⁸

Treatment of CNF (i) with the oxidant, $\text{NaMnO}_4 \cdot \text{H}_2\text{O}$, to generate composite (ii) increases rather than decreases the

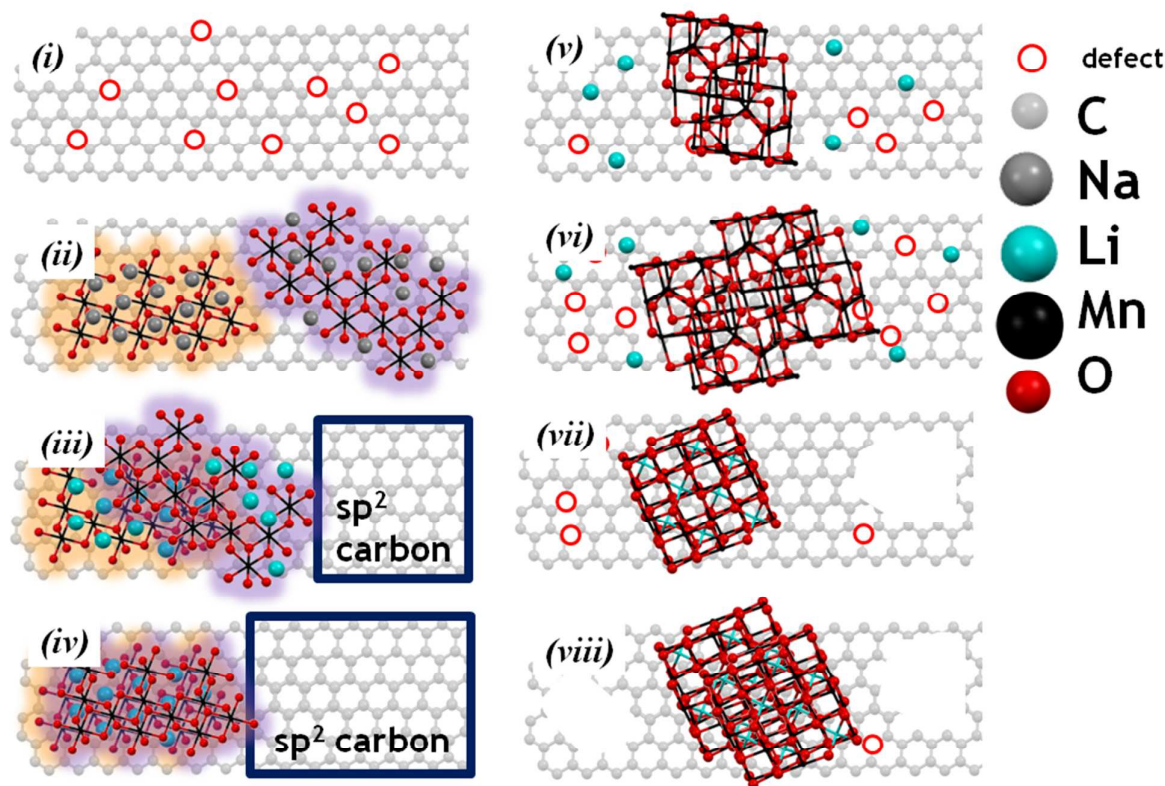


Fig. 5 A schematic of the order/disorder observed by the PXRD and Raman spectroscopic study of materials (i)–(viii). The unmodified CNF (i) contains defects; composite (ii) preferentially grafts birnessite AMnO_x at the defect sites. As the MnO_6 planes become more registered, relatively defect-free sp^2 carbon that does not ‘tether’ the MnO_6 sheets, becomes exposed for composites (iii) and (iv). As the lamellar AMnO_x grows into a 3D $\text{A}'\text{Mn}_2\text{O}_4$ spinel under argon, composites (v) and (vi), more defects are observed via Raman spectroscopy, attributable to breakage of C=C bonds during the mechanical stresses imposed by oxide transformation. Heating in air to produce composites (vii) and (viii) removes defects because defective carbon is preferentially pyrolyzed in the presence of oxygen and manganese oxide compared to graphitic carbon.

relative fraction of ordered carbon in CNF, as substantiated by its lower I_D/I_G ratio versus unmodified CNF (Fig. 4). Although the MnO_4^- anion can preferentially oxidize sp^2 carbon to generate C–O speciation (thereby increasing sp^3 content and disorder),³⁹ the disappearance of the 1195 cm^{-1} band indicates that the $\text{MnO}_4^-/\text{carbon}$ redox starts at defects in the CNF (thereby decreasing sp^3 content and disorder).

The time over which $\text{NaMnO}_x/\text{CNF}$ is exposed to aqueous LiNO_3 (8 h vs 24 h, respectively, to yield composites (iii) and (iv)) markedly affects the Raman signature of the carbon nanofoam substrate: the value of I_D/I_G progressively decreases, i.e., the incoming light scatters off carbon of higher graphitic content. Analysis of the surface elemental composition of $\text{NaMnO}_x/\text{CNF}$ by X-ray photoelectron spectroscopy (XPS), yields a C:Na atomic ratio of 0.32; immersion in the aqueous Li^+ solution suffices to fully exchange Li^+ for Na^+ such that composite (iii) has a C:Na ratio of 0.015 and composite (iv) has a C:Na ratio of 0.011 (see Supporting Information, Fig. S12[†]).

Converting disordered carbon to graphitic carbon simply by soaking a carbon nanofoam paper in aqueous salt solution, besides being energetically implausible, cannot explain the I_D/I_G trend because unmodified CNF soaked for 24 h in 1 M LiNO_3 at room temperature, rinsed well, and dried at 45°C has the same I_D/I_G as the starting CNF (Fig. 4). We ascribe the higher sp^2 content detectable post- Li^+ exchange, which further increases with increasing time in the salt solution, to a Li^+ electrostatically driven ordering of misaligned layers in the initial birnessite deposit generated by the rapid reaction of NaMnO_4 with carbon.

If any nanometric sheets of MnO_6 octahedra out of registry with the initial carbon nucleated sheet of MnO_6 octahedra move into alignment, more basal-plane sp^2 carbon would be unveiled. This mechanism would explain why $\text{LiMnO}_x[24]/\text{CNF}$ is the one birnessite composite that exhibits PXRD-observable crystalline registry of the layers. The PXRD and Raman indication of lamellar alignment in $\text{LiMnO}_x[24]/\text{CNF}$ is depicted schematically in Fig. 5.

Heat treatment of $\text{LiMnO}_x[24]/\text{CNF}$, composite (iv), under argon decreases the relative amount of sp^2 carbon coincident with phase conversion of the lamellar oxide to tetragonal Mn_3O_4 . An argon atmosphere lowers the partial pressure of oxygen (p_{O_2}), which should reduce oxygenates at the carbon surface, thereby making the carbon substrate look more sp^2 -like and further decreasing the I_D/I_G ratio. But physically lifting MnO_6 octahedra out of lamellar sheets into a tetragonal arrangement—building up the nanoscale oxide from 2D to 3D—should impose mechanical forces on the carbon floor.

Mechanically breaking C=C sp^2 bonds creates dangling bonds that would then getter trace oxygen present in the argon and paradoxically generate more sp^3 carbon, even at

low p_{O_2} . Composite (vi), which spent more time under the 300°C Ar conditions, shows an even higher I_D/I_G ratio. The tensile strength required to break multiwall carbon nanotubes is 1.4–2.9 GPa and the thermally driven synthesis of sp^3 -bonded cubic diamond from sp^2 -bonded graphite at $>1200\text{K}$ requires 6–7 GPa.^{40,41} The mechanical forces unleashed during phase conversion from a 2D arrangement of MnO_6 octahedra to a 3D arrangement would have to be on the order of a GPa to mechanically break C=C bonds present in the CNF to generate the dangling bonds that then getter trace oxygen. Scanning electron micrographs show that the nanofoam surface does roughen after heat treatment in Ar (Fig. S23[†]).

Heat treatment in air of composite (vi), which converts tetragonal Mn_3O_4 at the walls of the CNF to cubic LiMn_2O_4 spinel (composites (vii) and (viii)), reverses this trend to increasing disorder. The I_D/I_G ratio progressively decreases with time spent in air at 200°C , which indicates a relative increase in the content of ordered carbon in the CNF. Transition-metal oxides are known to catalyze the combustion of carbon, even at low calcination temperatures,⁴² with disordered carbon combusting before graphitic carbon.⁴³ Manganese oxides in particular have been used since the Middle Palaeolithic era—60,000 to 40,000 years ago—by Neanderthals to lower the auto-ignition temperature of wood.⁴⁴ Again an apparent paradox, but in this instance an oxidative treatment increases the fraction of sp^2 carbon.

The $200^\circ\text{C}/\text{air}$ -treated composites show a mass loss per cm^2 relative to the Ar-only heated composite (vi): 3.8% lost for composite (vii)/2 h and a 9% loss for composite (viii)/6 h; heat treatment in air further coarsens the composite surface, as seen by SEM (see Fig. S23[†]).

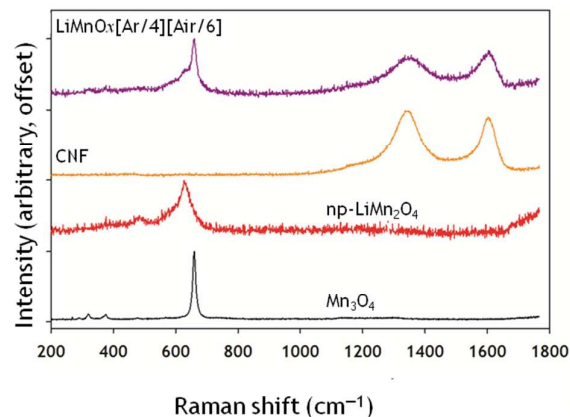


Fig. 6 The Raman spectra obtained for standards of crystalline Mn_3O_4 and nanoparticulate LiMn_2O_4 , and for CNF (i) and $\text{LiMnO}_x[\text{Ar}/4][\text{Air}/6]/\text{CNF}$ [composite (viii)]. Composite (viii) exhibits signals associated with LiMn_2O_4 , Mn_3O_4 , and the CNF, consistent with the DPDF and PXRD studies.

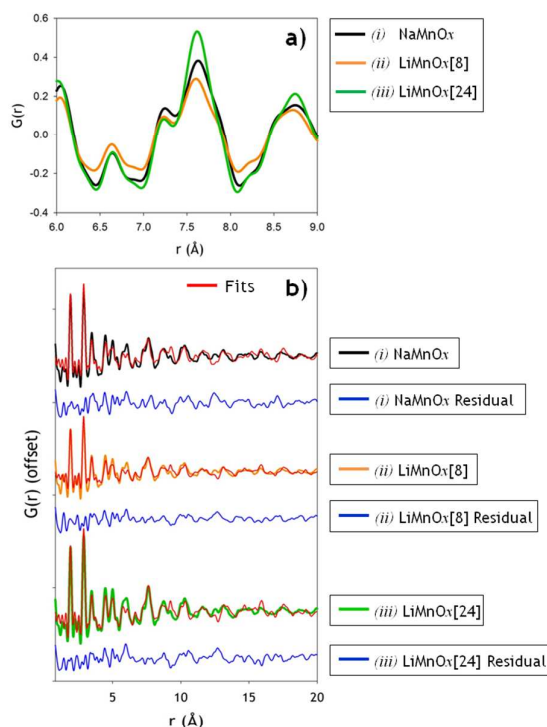


Fig. 7 a) The DPDF data of composites (ii)–(iv) with carbon contributions subtracted showing the correlations between $\text{MnO}_6 \cdots \text{MnO}_6$ sheets. An increase in sharpness indicates decreasing turbostratic disorder; this increase in lamellar order is observed with the appearance of a Bragg peak in the PXRD of the $\text{LiMnO}_x/\text{CNF}[24]$ composite. **b)** Fits of the unheated AMnO_x ($A = \text{Na}^+$, Li^+) to a birnessite phase that displays large disorder with ~ 4 -nm particle sizes. The data with fits and residuals in high resolution are provided in Supplementary Information, Figs. S27–S29.

The Raman scattering from Mn–O bonds in MnO_x phases occurs near 600 cm^{-1} and is weak for composites (ii)–(vii); see Fig. S11[†]. Composite (viii), however, shows a strong peak at 665 cm^{-1} with a broad peak centered at 630 cm^{-1} (Fig. 6). These peaks correlate with the scattering observed for LiMn_2O_4 and Mn_3O_4 standards in agreement with the phase assignments derived from PXRD and DPDF analyses.

3.3 Analysis of multiphase structure with synchrotron X-ray total scattering methods

The PXRD and Raman scattering studies of MnO_x -painted carbon nanofoam paper provide qualitative insight into the structural and physical changes within this 3D microheterogeneous composite as the nanoscale oxide undergoes transformation from lamellar birnessite to cubic spinel. To establish a quantitative understanding of this

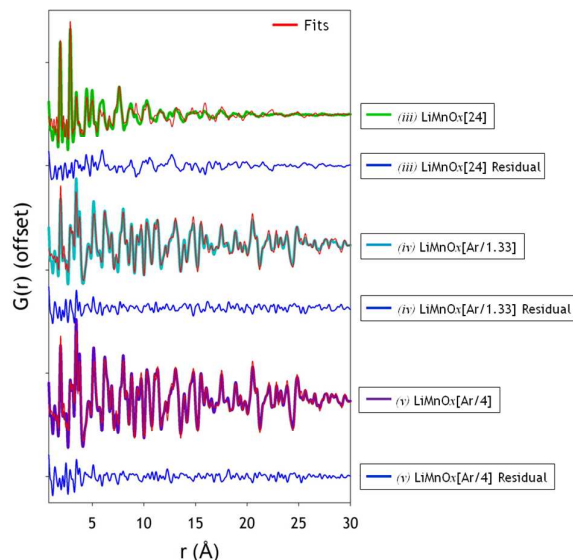


Fig. 8 The DPDF data of composites (iv)–(vi) with carbon contributions subtracted. A large increase in order is immediately observed upon heating the composite in argon for 1.33 h, as seen by peaks in $G(r)$ persisting at $r > 15 \text{ Å}$. The data for composites (v) and (vi) fit to a structure of hausmannite Mn_3O_4 with a trace of cubic LiMn_2O_4 . The data with fits and residuals in high resolution are provided in Supplementary Information, Figs. S29–S31.

complex system, we turned to ex-situ DPDF. The use of total scattering analyses overcomes limitations arising from the broad Bragg peaks characteristic of nanoscale materials—in particular broad peaks seen with disordered and amorphous materials. During workup of the total scattering data, scale factors can be used to subtract contributions from the supporting substrate; this approach is designated differential pair distribution function (DPDF) and thin-film pair distribution function (TFPDF).^{11,30,31}

We demonstrate that the power of TFPDF works in 3D as well, allowing us to null out the carbon signal from the nanofoam paper to quantify explicitly the structure of the semi-crystalline manganese oxide nanoscopic paint. Modeling the MnO_x systems without crystallographic constraints (such as with Reverse Monte Carlo approaches) would provide greater fitness compared to crystallographically constrained models;⁴⁵ however, RMC methods for the composite multiphase CNF + MnO_x systems we study herein would require large numbers of refineable variables for the 2D r vs. $G(r)$ DPDF data obtained. Crystallographic models—modeled via PDFGui—provide tractable solutions for these complex systems.

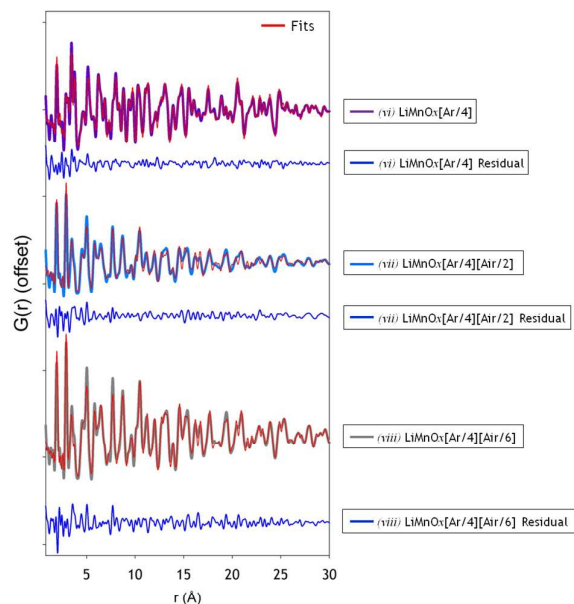


Fig. 9 The DPDF data and fits of composites (vi)–(viii) after subtraction of the carbon signal. Heating composite (vi) in air for 2 h decreases crystallinity—as observed by decrease in $G(r)$ at $r > 15$ Å—as the material is transformed from predominantly nanoscopic tetragonal hausmannite to predominantly nanoscopic cubic LiMn_2O_4 . The data with fits and residuals in high resolution are provided in Supplementary Information, Figs. S31–S33.

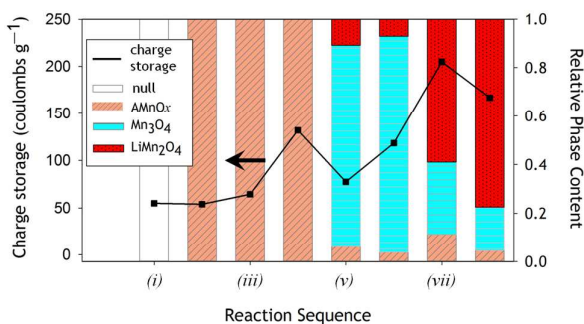


Fig. 10 Charge storage in MnO_x @CNF composite electrodes as a function of reaction 'step' over the potential range (3.05–4.35 V vs. Li/Li^+). The histogram represents relative phase content of the manganese oxide on the CNF; the values along the x axis correspond to the composites depicted in Fig. 1. As the composite is processed, the phase fraction of LiMn_2O_4 increases with a concomitant increase in charge storage; a peak is observed in the charge storage with composite (iv), $\text{LiMnO}_x[24]$ @CNF when the composite contains registered MnO_6 sheets.

After removing the carbon contribution to the total scattering and processing the DPDF data, model structures are fitted to the corrected data (described in Experimental Methods) for the MnO_x @CNF series (Figs. 7–9). The individual

fits of the DPDF data are shown in the Supplementary information (Figs S27–S33); the DPDF fit parameters and details are provided in Tables S4–S10 and S12. The lamellar AMnO_x @CNF series, composites (ii)–(iv), are fitted to a cation-compensated birnessite structure in agreement with previous transmission electron micrographic and XAS examinations of Na^+ -compensated lamellar MnO_x -modified CNF.^{1,2} To account for turbostratic disorder of the lamellar AMnO_x , a parameter to increase the anisotropic displacement parameter along the c axis was employed. This variation allowed an appropriate fit with low residual values and minimal variables.

The features in the DPDF, $G(r)$, as a function of radius (r) extend to ~ 40 Å for all three lamellar composites. To a first approximation, all three lamellar composites are structurally similar, with the patterns fit to a modelled spheroidal structure of highly disordered, ~ 4 -nm birnessite particles comprising six sheets of MnO_6 octahedra. Although DPDF analyses typically determine exact particle size, the high degree of disorder required to fit the DPDF data makes the 4-nm assignment of average particle size only semi-quantitative. For composite (iv), the topotactic end product, $\text{LiMnO}_x[24]$ @CNF, the lamellar spacing refines to 6.75 Å, in agreement with the (001) spacing observed by PXRD (see Fig. 2 and Table S7). The DPDF of $\text{LiMnO}_x[24]$ @CNF, composite (iv), has sharper peaks relative to the DPDF of $\text{LiMnO}_x[8]$ @CNF, composite (iii). This improved line shape is particularly true for interlayer spacing correlations at ~ 7.5 Å (Fig. 7a). The sharper peaks indicate increased crystallinity as the birnessite sheets come into greater registry. This registry is semi-quantitatively observed in fits of the DPDF: the turbostratic disorder term remains similar for NaMnO_x @CNF and $\text{LiMnO}_x[8]$ @CNF, but the term decreases for $\text{LiMnO}_x[24]$ @CNF relative to NaMnO_x @CNF and $\text{LiMnO}_x[8]$ @CNF.

The topotactic end product for the lamellar series, composite (iv), was then heated at 300 °C in argon for either 1.33 h or 4 h to synthesize composites (v) and (vi), respectively. The ex-situ DPDF of these MnO_x -modified CNFs, show much greater crystallinity, as seen by sharper peaks in the $G(r)$ - r pattern, with the $G(r)$ intensity extending to 100 Å (Fig. 8). The cell parameters are similar to standards of 50:50 mixtures of nanocrystalline LiMn_2O_4 :CNF and crystalline Mn_3O_4 :CNF that were processed as the composites were to generate DPDFs (see Fig. S25 and Fig. S26[†]). Models of (v) and (vi) were evaluated with cubic and tetragonal structures plus birnessite LiMnO_x and converged to the best fit for a tetragonal phase, consistent with hausmannite Mn_3O_4 with a $\sim 10\%$ birnessite contribution. To minimize variables, the birnessite contribution was refined with use of the structure of the most crystalline birnessite, $\text{LiMnO}_x[24]$, and refinement of the relative content of the birnessite. The particle size obtained by DPDF refinements of the tetragonal phase of composites (v) and (vi) is ~ 10 nm, consistent with the PXRD size estimate.

The question then becomes what is the fate of the interlayer Li^+ present at 0.38 Li per Mn in $\text{LiMnO}_x[24]$ @CNF1 as the birnessite structure is transformed into an un lithiated tetragonal phase? The minor fraction of unreacted birnessite

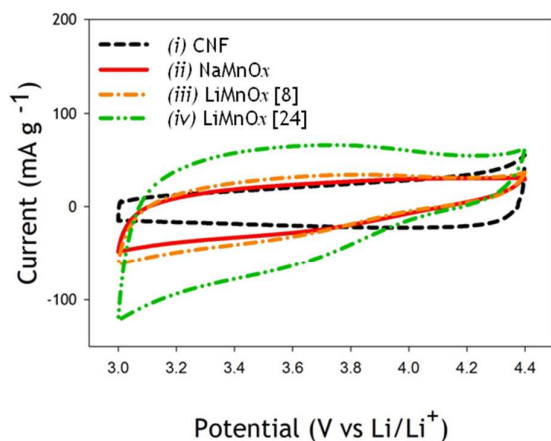


Fig. 11 Cyclic voltammetry at 0.5 mV s^{-1} in $\text{LiPF}_6/\text{EC-DC-DMC}$ electrolyte of a bare CNF and $\text{NaMnO}_x/\text{CNF}$ (composite (ii)), $\text{LiMnO}_x[8]/\text{CNF}$ (composite (iii)) and $\text{LiMnO}_x[24]/\text{CNF}$ (composite (iv)). The current is normalized to the mass of the total composite electrode.

LiMnO_x present in the argon-heated composite can only account for ~ 0.06 Li per Mn. Low-intensity peaks present at low r in the DPDF $G(r)$ cannot be fit to MnO_x , but do fit short-range Li–O correlations. These peaks cannot be refined with models of nanocrystalline LiOH , Li_2O , or LiO , indicating that the nature of the extruded $\text{LiO}_x/\text{LiO}_x\text{H}_y$ component is nanoscopic and highly disordered. Our previous study of $\text{LiMnO}_x[\text{Ar}/4]/\text{CNF}$ by ^7Li NMR also demonstrated the existence of MnO_x -unincorporated Li^+ ions.¹

The $\text{LiMnO}_x[\text{Ar}/4]/\text{CNF}$ (composite (vi)) was then rapidly heated in static air by placing it directly into a 200°C -furnace for 120 min. The DPDF analysis of this composite (vii) indicates that the mixed tetragonal $\text{MnO}_x/\text{birnessite}$ phases of (vi) convert to predominantly cubic spinel LiMn_2O_4 with some hausmannite Mn_3O_4 retained (Fig. 9); the fit that yielded the lowest residual again contained a contribution of $\sim 10\%$ birnessite LiMnO_x (Fig. 10). Calcining a separate sample of $\text{LiMnO}_x[\text{Ar}/4]/\text{CNF}$ for 360 min yielded the final composite in the series, (viii), which was again a multiphase blend of LiMn_2O_4 , Mn_3O_4 , and the ever-persistent $\sim 10\%$ birnessite contribution (Fig. 9 and Fig. 10).

The heat treatment in argon is therefore analogous to a ceramic reaction that yields phase-separated solids, in this case Mn_3O_4 and LiO_xH_y . The subsequent heating of the nanoparticulate materials in air, nominally still in intimate contact, creates the desired LiMn_2O_4 -based composites (vii) and (viii). This soft treatment in a low partial pressure of oxygen at low temperature has previously been used to lithiate mesoporous $\beta\text{-MnO}_2$ to obtain mesoporous LiMn_2O_4 in the absence of a carbon phase.⁴⁶ Such a methodology could be applied to other oxide nanoparticulate materials to create desired lithiated architectures for electrochemical usage.

The phase evolution of MnO_x can be quantified by the DPDF analyses as the reaction series transforms the oxide from birnessite \rightarrow hausmannite \rightarrow lithiated spinel, allowing us to

establish the fraction of each MnO_x component in the respective composite (Fig. 10). Of note is the fact that for all argon- and air-treated MnO_x/CNF composites, the models that best fit the DPDF data include a fractional inclusion of a lamellar structure at $\sim 10\%$. We posit that this persistent feature reflects not a segregated phase, but a key construction element as the nanoscale MnO_x reconfigures from a nanometric, \sim six layer-thin 2D crystal into MnO_6 octahedra rising up into a 3D arrangement.

The electroless deposition of nanoparticulate manganese oxide phases to generate MnO_x/CNF is initiated as the permanganate oxidant attacks the sacrificial reductant, namely the walls of the carbon nanofoam. The surface of the carbon seemingly serves as an epitaxial template for a 2D layered arrangement of MnO_6 octahedra in that we only find the lamellar phase in permanganate-exposed CNFs regardless of whether the cation accompanying MnO_4^- is Li^+ , Na^+ , or K^+ . Without a carbon support, permanganate oxidation of an organic reductant in isotropic media templates nonlamellar phases, e.g., cryptomelane for KMnO_4 .^{47,48} In isotropic media, the effect of synthetic temperature, pH, and molar ratios of $\text{MnO}_4^-/\text{Mn}^{2+}$ has been analyzed to establish three crystallization stages (induction, fast crystallization, steady-state) of sodium birnessites. Modification of the synthetic conditions affects the resulting structure of MnO_x .⁴⁹ In the absence of carbon substrates, fast permanganate oxidation reactions result in layered morphologies while slower reactions produce tunneled MnO_x phases.²⁰ These kinetics likely carry over to interactions with carbon: the surface of the carbon nanofoams reacts quickly with the permanganate ion employed and results in layered AMnO_x phase(s) that act as a seed for the remaining permanganate to crystallize in a layered manner. We note that permanganate oxidation under anisotropic conditions, such as that at the walls of CNF, yields disordered birnessite AMnO_x whether the A cation arrives as NaMnO_4^1 or KMnO_4^2 .

We propose that the redox product left behind after MnO_4^- oxidizes carbon at the nanofoam wall, i.e., the first, nucleating sheet of MnO_6 octahedra, remains permanently affixed to the carbon and serves as the foundation onto which the tetragonal and cubic architectures are built from MnO_6 construction materials harvested from sheets of MnO_6 above the base plate. In this reaction scheme, the bottom layer out of the six that comprise each $\text{LiMnO}_x \sim 4\text{-nm}$ birnessite particle will always be present as the new crystal phases are constructed atop it. One layer out of six would represent $\sim 15\%$ of the MnO_x crystal speciation, not coincidentally comparable to the $\sim 10\%$ fraction assigned by the DPDF fits.

Although the Raman intensities show a change in the order/disorder of the carbon nanofoam backbone upon processing from CNF (i) to $\text{LiMnO}_x[\text{Ar}/4][\text{Air}/2]/\text{CNF}$ (viii), the change is minimal to the structure of the carbon. The Raman intensity of the series varies from $I_b/I_g = 0.95 \pm 12.5\%$; modification of the scale factor to correct for structural carbon contributions to the DPDF $\pm 12.5\%$ shows little variation in the DPDFs of composites (ii)–(viii), see Figs. S30–S36. This number

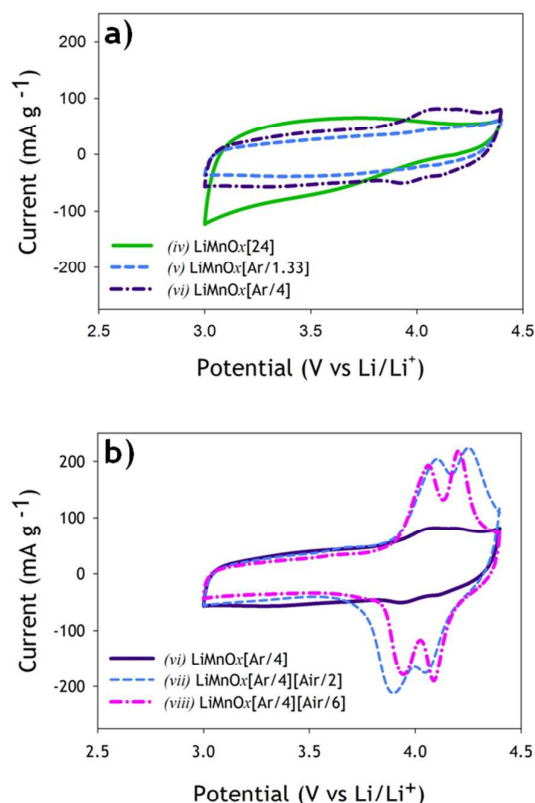


Fig. 12 Cyclic voltammetry at 0.5 mV s^{-1} in $\text{LiPF}_6/\text{EC-DC-DMC}$ electrolyte of **a)** $\text{LiMnO}_x[24]@\text{CNF}$ and composites heated in argon $\text{LiMnO}_x[\text{Ar}/1.33]@\text{CNF}$ (v) and $\text{LiMnO}_x[\text{Ar}/4]$ (vi) and **b)** (v) $\text{LiMnO}_x[\text{Ar}/4]$ and composites heated in argon/air $\text{LiMnO}_x[\text{Ar}/4][\text{Air}/2]$ (vii) and $\text{LiMnO}_x[\text{Ar}/4][\text{Air}/6]$ (viii). The current is normalized to the mass of total composite electrode.

is a conservative estimate: changes in the X-ray scattering are relatively small compared to changes in Raman scattering

3.4 Electrochemistry

With a structural framework in hand for the lamellar \rightarrow tetragonal \rightarrow cubic series of $\text{MnO}_x@\text{CNFs}$, we turned to a structure–property study and evaluated the electrochemical character of the various composites by cyclic voltammetry (CV) in nonaqueous electrolyte. Over 3.0–4.4 V (vs Li/Li^+), the native CNF and the three birnessite composites ((ii)–(iv)) exhibit the rectangular current–potential (i – V) voltammetric response characteristic of an electrochemical capacitor (Fig. 11). As normalized to the weight of the electrode, the charge stored at the unmodified CNF, $\text{NaMnO}_x@\text{CNF}$, or $\text{LiMnO}_x[8]@\text{CNF}$ is comparable (54.9 C g^{-1} for the CNF; 59.2 C g^{-1} , for birnessite-painted composites (ii) and (iii)). Running the topotactic exchange of Li^+ for Na^+ for 24 h rather than 8 h doubles the charge stored by $\text{LiMnO}_x[24]@\text{CNF}$ to 131.8 C g^{-1} . Coating the CNF with disordered AMnO_x was insufficient to increase the nonaqueous pseudocapacitive charge storage of the material; registry of the birnessite MnO_6 slabs is necessary.

Our previous report of the electrochemical character of the $\text{MnO}_x@\text{CNF}$ lamellar \rightarrow tetragonal \rightarrow cubic series was performed in neutral pH aqueous electrolyte. Under those conditions, the $\text{NaMnO}_x@\text{CNF}$ (ii) and $\text{LiMnO}_x[24]@\text{CNF}$ (iv) composite electrodes displayed identical capacitive behavior.¹ However, subsequent in-situ characterization using electrochemical quartz crystal microbalance measurements revealed that charge-storage in aqueous electrolytes at $\text{NaMnO}_x@\text{CNF}$ is dominated by anion-association mechanisms rather than the expected cation-insertion reactions.⁵⁰ In aqueous electrolytes, the hydration shells and counterions surrounding the alkali cation present a significant entropic barrier to insertion/intercalation processes, such that anion-based pseudocapacitance mechanisms may be energetically preferred. In nonaqueous media where the solvents, such as the alkyl carbonates, offer only modest donicity to solvate Li^+ , conventional cation-insertion mechanisms are more likely to dominate the oxidation–reduction processes at the MnO_x .

The unimpressive charge-storing response exhibited by birnessite $\text{NaMnO}_x@\text{CNF}$ (ii) and $\text{LiMnO}_x[8]@\text{CNF}$ (iii) matches the few reports in the literature for the response of birnessite MnO_x in nonaqueous electrolytes.⁵¹ Of note is the marked enhancement in the amount of charge stored at $\text{LiMnO}_x[24]@\text{CNF}$ (iii), the composite electrode in which the lamellar structure of the nanometric MnO_x deposit comes into registry. Fulfilling topotactic replacement of Na^+ by Li^+ in the birnessite by ion exchange is not sufficient alone to create this increased capacitance: the identity of the alkali ion matters as does time of exposure in the concentrated salt solution. Taken together, we suggest that the hydrated Li^+ (600 pm^3 in size with >10 waters of hydration) serves as the lubricant by which the turbostratic disorder of the MnO_6 sheets is annealed over 24 h to exhibit lamellar registry.

The alkali ions Na^+ and Li^+ differ in both chemical hardness as well as the number of waters of hydration that solvate the ion; hydrated Na^+ is roughly one-third smaller at $\sim 400 \text{ pm}^3$.⁵² Fully exchanged $\text{LiMnO}_x[8]@\text{CNF}$ is indistinguishable from $\text{NaMnO}_x@\text{CNF}$ by the degree of PXRD- and DPDF-discernible structural disorder, the DPDF-derived interlamellar spacing correlations ($\sim 7.5 \text{ \AA}$, see Fig. 7a), and the capacity to store electrochemical charge in nonaqueous electrolyte. The slight improvement in the relative content of graphitic, sp^2 carbon seen in the Raman-derived I_D/I_G ratio for $\text{LiMnO}_x[8]@\text{CNF}$ over that of $\text{NaMnO}_x@\text{CNF}$ indicates the alignment process has started after Li^+ exchanges for Na^+ , but that 8 h is insufficient to yield registry.

The greater lamellar registry of LiMnO_x observed by PXRD and DPDF for $\text{LiMnO}_x[24]@\text{CNF}$ offers the likely explanation for the distinctive electrochemistry expressed by this composite electrode. Registered sheets of MnO_6 octahedra should establish the shortest distance between Mn sites in one sheet to Mn sites in an adjacent sheet and thereby facilitate interlamellar electron self-exchange between Mn^{4+} and Mn^{3+} sites (intralamellar electron self-exchange should be comparably fast in disordered or registered birnessite sheets). The coupled processes of electron hopping and ion diffusion characteristic of mixed-valent redox films⁵³ drives the ability to

store charge in the birnessite deposits. The Mn content in the composite electrode is more effectively sampled when the nanometric sheets of MnO₆ octahedra are aligned rather than rotationally or turbostratically disordered, likely because the disorder forces longer electron hopping distances for some fraction of the Mn sites in each nanoparticle.

For argon- and air-heated MnO_x@CNF composites, two redox peaks begin to emerge from the capacitive background (Fig. 12) at potentials characteristic of lithiating cubic LiMn₂O₄ spinel in nonaqueous electrolytes; these redox processes are assigned to Li⁺ insertion/extraction into the tetrahedral sites of LiMn₂O₄ commensurate with Mn⁴⁺/Mn³⁺ redox.⁵⁴ Heating LiMnO_x[24]@CNF, composite (iv), in an argon atmosphere maintains the pseudocapacitive envelope over 3.0–3.8 V vs Li/Li⁺, but peaks centered at ~4.0 V begin to appear above the capacitive background. Heating the material in air generates a LiMn₂O₄-enriched oxide (Fig. 10).

Heating LiMnO_x[Ar/4]@CNF in air for 4 h rather than 2 h increases the DPDF-established content of LiMn₂O₄ relative to Mn₃O₄ (Fig. 10), but decreases the overall charge storage for the LiMn₂O₄-richer composite (viii). The DPDF analysis indicates why: the particle size of both LiMn₂O₄ and Mn₃O₄ phases increases with extended heat treatment in air (Fig. 9). The particle size of the active LiMn₂O₄ phase increases from ~3.3 nm in composite (vii) to ~5.7 nm for composite (viii). Despite the increase in the fractional content of battery-relevant LiMn₂O₄ for composite (viii) relative to composite (vii), the decrease in surface area for (viii) decreases pseudocapacitive contributions to the charge-storage envelope from 3.0–4.4 V (Fig. 11). This loss of pseudocapacitance is most apparent over the region 3.0–3.8 V, which lacks Faradaic features. Strong Faradaic features more than compensate for the decreased pseudocapacitance thereby providing the greatest amount of charge storage for composite (vii), LiMnO_x[Ar/4][Air/2], amongst the series of (i)–(viii). As observed in the Raman analysis, the amount of disordered carbon is also lessened from air treatment. The engineering of composites is therefore not confined to the phase type of the oxide but also its expression as an oxide@carbon architecture. Careful treatments—such as the use of gradual heating rates, mild environments, and mild redox reagents—must be carefully examined and employed to arrive at a desired phase and form.

Conclusions

We have shown that the topotactical system of MnO_x proceeds through multiple phases with a particular synthetic scheme and cannot be understood as a single-phase material. Furthermore, alteration of composite materials adjusts several components at a time (such as both the multiphase manganese oxide system and the carbon support) and multiple techniques are needed in order to probe the changes within the composite structure. The combination of analyses revealed new structural understanding of the electrode material: (i) MnO₆ slabs within birnessite LiMnO_x are aligned by immersion in an aqueous Li⁺ solution and afford increased nonaqueous

pseudocapacitance, (ii) construction of the 3D extended MnO_x phases are built upon a foundation slab of lamellar MnO, (iii) extensive oxidation creates large nanoparticles of LiMn₂O₄ and incomplete conversion of Mn₃O₄ to LiMn₂O₄, and (iv) the carbon nanofoam scaffold that supports the nanoscale MnO_x overlayer is not a passive observer as the oxide is phase converted. Care must be taken to engineer (nano)composites, such as the use of gradual heat rates, judicious choice of heating environments, and lengths of heat treatments, e.g., heat rates on the order of 1°C min⁻¹ to 200–300°C.

Differential pair distribution function analyses offer a powerful tool to examine changes on the atomistic level with subtraction of background signals that obscure traditional scattering techniques, FTIR, and/or UV–Vis–NIR methods. With an understanding of the specific phases present, electrochemical performance of complex composite materials can be correlated with phases and architectural arrangements that contribute to a specific charge-storage mechanism.

Acknowledgements

This work was supported by the U.S. Office of Naval Research. M. D. D. acknowledges the National Research Council for a Postdoctoral Fellowship (2014–2017). This research used resources of the Advanced Photon Source (APS), a U.S. Department of Energy (DOE) Office of Science User Facility operated for the DOE Office of Science by Argonne National Laboratory under Contract No. DE-AC02-06CH11357. The PDF experiments were conducted at 11-ID-B of the APS. A synchrotron PXRD pattern was obtained via the mail-in program at 11-BM of the APS. We thank Dr. Mikhail Feygenson (Oak Ridge National Laboratory) and the 11-ID-B/NOMAD partner program for initial data collection of pair distribution function data.

Notes and references

- M. B. Sassin, S. G. Greenbaum, P. E. Stallworth, A. N. Mansour, B. P. Hahn, K. A. Pettigrew, D. R. Rolison and J. W. Long, Achieving Electrochemical Capacitor Functionality from Nanoscale LiMn_2O_4 Coatings on 3-D Carbon Nanoarchitectures, *J. Mater. Chem. A*, 2013, **1**, 2431–2440.
- A. E. Fischer, M. P. Saunders, K. A. Pettigrew, D. R. Rolison, and J. W. Long, Electroless Deposition of Nanoscale MnO_2 on Ultraporos Carbon Nanoarchitectures: Correlation of Evolving Pore–Solid Structure and Electrochemical Performance *J. Electrochem. Soc.*, 2008, **155**, A246–A252.
- J. W. Long and D. R. Rolison, Architectural Design, Interior Decoration, and Three-Dimensional Plumbing en Route to Multifunctional Nanoarchitectures, *Acc. Chem. Res.*, 2007, **40**, 854–862.
- J. Baxter, Z. Bian, G. Chen, D. Danielson, M. S. Dresselhaus, A. G. Fedorov, T. S. Fisher, C. W. Jones, E. Maginn, U. Kortshagen, A. Manthiram, A. Nozik, D. R. Rolison, T. Sands, L. Shi, D. Sholl, and Y. Wu, Nanoscale Design to Enable the Revolution in Renewable Energy, *Energy Environ. Sci.*, 2009, **2**, 559–588.
- J. R. Szczech and S. Jin, Nanostructured Silicon for High Capacity Lithium Battery Anodes, *Energy Environ. Sci.*, 2011, **4**, 56–72.
- X. Rui, H. Tan, and Q. Yan, Nanostructured Metal Sulfides for Energy Storage, *Nanoscale*, 2014, **6**, 9889–9924.
- W. Dmowski, T. Egami, K. E. Swider-Lyons, C. T. Love, and D. R. Rolison, Local Atomic Structure and Conduction Mechanism of Nanocrystalline Hydrous RuO_2 from X-ray Scattering, *J. Phys. Chem. B*, 2002, **106**, 12677–12683.
- P. J. Chupas, X. Qiu, J. C. Hanson, P. L. Lee, C. P. Grey, and S. J. L. Billinge, Rapid-Acquisition Pair Distribution Function (RA-PDF) Analysis, *J. Appl. Crystallogr.*, 2003, **36**, 1342–1347.
- W. Dmowski, T. Egami, E. Swider-Lyons, W.-F. Yan, S. Dai, and S. H. Overbury, Local Atomic Structure in Disordered and Nanocrystalline Catalytic Materials, *Z. Kristallogr.*, 2007, **222**, 617–624.
- S. J. L. Billinge, Nanoscale Structural Order from the Atomic Pair Distribution Function (PDF): There's Plenty of Room in the Middle, *J. Solid State Chem.*, 2008, **181**, 1695–1700.
- K. M. Ø. Jensen, A. B. Blichfeld, S. R. Bauers, S. R. Wood, E. Dooryhee, D. C. Johnson, B. B. Iversen, and S. J. L. Billinge, Demonstration of Thin Film Pair Distribution Function Analysis (TFPDF) for the Study of Local Structure in Amorphous and Crystalline Thin Films, *IUCrJ*, 2015, **2**, 481–489.
- N. Yamakawa, M. Jiang, B. Key, and C. P. Grey, Identifying the Local Structures Formed during Lithiation of the Conversion Material, Iron Fluoride, in a Li Ion Battery: A Solid-State NMR, X-ray Diffraction, and Pair Distribution Function Analysis Study, *J. Am. Chem. Soc.*, 2009, **131**, 10525–10536.
- F. Pourpoint, X. Hua, D. S. Middlemiss, P. Adamson, D. Wang, P. G. Bruce, and C. P. Grey, New Insights into the Crystal and Electronic Structures of $\text{Li}_{1+x}\text{V}_{1-x}\text{O}_2$ from Solid State NMR, Pair Distribution Function Analyses, and First Principles Calculations, *Chem. Mater.*, 2012, **24**, 2880–2893.
- T. R. Welberry and T. Weber, One Hundred Years of Diffuse Scattering, *Crystallogr. Rev.*, 2016, **22**, 2–78.
- A. J. Bard, H. D. Abruna, C. E. D. Chidsey, L. R. Faulkner, S. W. Feldberg, K. Itaya, M. Majda, O. Melroy and R. W. Murray, The Electrode/Electrolyte Interface—A Status Report, *J. Phys. Chem.*, 1993, **97**, 7147–7173.
- K. M. Wiaderek, O. J. Borkiewicz, E. Castillo-Martínez, R. Robert, N. Pereira, G. G. Amatucci, C. P. Grey, P. J. Chupas, and K. W. Chapman, Comprehensive Insights into the Structural and Chemical Changes in Mixed-Anion FeOF Electrodes by Using Operando PDF and NMR Spectroscopy, *J. Am. Chem. Soc.*, 2013, **135**, 4070–4078.
- T. Egami and S. J. L. Billinge, *Underneath the Bragg Peaks Structural Analysis of Complex Materials*; 2 ed.; Pergamon, 2003.
- H. D. Abruña, *Electrochemical Interfaces: Modern Techniques for In-Situ Interface Characterization*; VCH Pub, 1991.
- P. Lu, C. Li, E. W. Schneider, and S. J. Harris, Chemistry, Impedance, and Morphology Evolution in Solid Electrolyte Interphase Films during Formation in Lithium Ion Batteries, *J. Phys. Chem. C*, 2014, **118**, 896–903.
- V. Petkov, Y. Ren, I. Saratovsky, P. Pastén, S. J. Gurr, M. A. Hayward, K. R. Poeppelmeier, and J. F. Gaillard, Atomic-Scale Structure of Biogenic Materials by Total X-ray Diffraction: A Study of Bacterial and Fungal MnO_x , *ACS Nano*, 2009, **3**, 441–445.
- M. Zhu, C. L. Farrow, J. E. Post, K. J. T. Livi, S. J. L. Billinge, M. Ginder-Vogel, and D. L. Sparks, Structural Study of Biotic and Abiotic Poorly-Crystalline Manganese Oxides Using Atomic Pair Distribution Function Analysis, *Geochim. Cosmochim. Acta*, 2012, **81**, 39–55.
- M. Huynh, C. Shi, S. J. L. Billinge, and D. G. Nocera, Nature of Activated Manganese Oxide for Oxygen Evolution, *J. Am. Chem. Soc.*, 2015, **137**, 14887–14904.
- I. Abidat, N. Bouchenafa-Saib, A. Habrioux, C. Comminges, C. Canaff, J. Rousseau, T. W. Napporn, D. Dambournet, O. Borkiewicz, and K. B. Kokoh, Electrochemically Induced Surface Modifications of Mesoporous Spinel ($\text{Co}_3\text{O}_{4-\delta}$, $\text{MnCo}_2\text{O}_{4-\delta}$, $\text{NiCo}_2\text{O}_{4-\delta}$) as the origin of the OER Activity and Stability in Alkaline Medium, *J. Mater. Chem. A*, 2015, **3**, 17433–17444.
- W.-S. Yoon, C. P. Grey, M. Balasubramanian, X.-Q. Yang, and J. McBreen, In Situ X-ray Absorption Spectroscopic Study on $\text{LiNi}_{0.5}\text{Mn}_{0.5}\text{O}_2$ Cathode Material during Electrochemical Cycling, *Chem. Mater.*, 2003, **15**, 3161–3169.
- H. Arai, K. Sato, Y. Orikasa, H. Murayama, I. Takahashi, Y. Koyama, Y. Uchimoto, and Z. Ogumi, Phase Transition Kinetics of $\text{LiNi}_{0.5}\text{Mn}_{1.5}\text{O}_4$ Electrodes Studied by in situ X-ray

- Absorption Near-Edge Structure and X-Ray Diffraction Analysis, *J. Mater. Chem. A*, 2013, **1**, 10442–10449.
- 26 J. W. Long, M. B. Sassin, A. E. Fischer, D. R. Rolison, A. N. Mansour, V. S. Johnson, P. E. Stallworth, and S. G. Greenbaum, Multifunctional MnO₂-Carbon Nanoarchitectures Exhibit Battery and Capacitor Characteristics in Alkaline Electrolytes, *J. Phys. Chem. C*, 2009, **113**, 17595–17598.
- 27 R. W. Pekala, J. C. Farmer, C. T. Alivisio, T. D. Tran, S. T. Mayer, J. M. Miller, and B. Dunn, Carbon Aerogels for Electrochemical Applications, *J. Non-Cryst. Solids*, 1998, **225**, 74–80.
- 28 J. C. Lytle, J. M. Wallace, M. B. Sassin, A. J. Barrow, J. W. Long, J. L. Dysart, C. H. Renninger, M. P. Saunders, N. L. Brandell, and D. R. Rolison, The Right Kind of Interior for Multifunctional Electrode Architectures: Carbon Nanofoam Papers with Aperiodic Submicrometre Pore Networks Interconnected in 3D. *Energy Environ. Sci.*, 2011, **4**, 1913–1925.
- 29 B. H. Toby and R. B. Von Dreele, GSAS-II: The Genesis of a Modern Open-Source All Purpose Crystallography Software Package, *J. Appl. Crystallogr.* 2013, **46**, 544–549.
- 30 P. J. Chupas, K. W. Chapman, G. Jennings, P. L. Lee, C. P. Grey, Watching Nanoparticles Grow: The Mechanism and Kinetics for the Formation of TiO₂-Supported Platinum Nanoparticles, *J. Amer. Chem. Soc.*, 2007, **129**, 12822–13824.
- 31 W. Li, R. Harrington, Y. Tang, J. D. Kubicki, M. Aryanpour, R. J. Reeder, J. B. Parise, and B. L. Phillips, Differential Pair Distribution Function Study of the Structure of Arsenate Adsorbed on Nanocrystalline γ -Alumina, *Environ. Sci. Technol.*, 2011, **45**, 9687–9692.
- 32 A. P. Hammersley, S. O. Svensson, M. Hanfland, A. N. Fitch, and D. Hausermann, Two-Dimensional Detector Software: From Real Detector to Idealised Image or Two-Theta Scan, *High Pressure Res.*, 1996, **14**, 235–248.
- 33 P. Juhás, T. Davis, C. L. Farrow, S. J. L. Billinge, PDFgetX3: A Rapid and Highly Automatable Program for Processing Powder Diffraction Data into Total Scattering Pair Distribution Functions, *J. Appl. Cryst.*, 2013, **46**, 560–566.
- 34 C. L. Farrow, P. Juhás, J. W. Liu, D. Bryndin, E. S. Božin, J. Bloch, T. Proffen, and S. J. L. Billinge, PDFfit2 and PDFgui: Computer Programs for Studying Nanostructure in Crystals, *J. Phys. Condens. Mat.* 2007, **19**, 335219–335226.
- 35 J. W. Long, R. M. Stroud, and D. R. Rolison, Controlling the Pore–Solid Architecture of Mesoporous, High Surface-Area Manganese Oxides with the Birnessite Structure, *J. Non-Cryst. Solids*, 2001, **285**, 288–294.
- 36 A. C. Ferrari and J. Robertson, Interpretation of Raman Spectra of Disordered and Amorphous Carbon, *Phys. Rev. B*, 2000, **61**, 14095–14107.
- 37 M. S. Dresselhaus, A. Jorio, M. Hofmann, G. Dresselhaus, and R. Saito, Perspectives on Carbon Nanotubes and Graphene Raman Spectroscopy, *Nano Lett.*, 2010, **10**, 751–758.
- 38 J. D. Wilcox, M. M. Doeff, M. Marcinek, R. Kostecki, Factors Influencing the Quality of Carbon Coatings on LiFePO₄. *Electrochem. Soc.* 2007, **154**, A389–A395.
- 39 M. Kim, C. K. Hong, S. Choe, and S. E. Shim, Synthesis of Polystyrene Brush on Multiwalled Carbon Nanotubes Treated with KMnO₄ in the Presence of a Phase-Transfer Catalyst, *J. Polym. Sci. A: Polym. Chem.*, 2007, **45**, 4413–4420.
- 40 M. F. Yu, O. Louire, M. J. Dyer, K. Moloni, T. F. Kelly, and R. S. Ruoff, Strength and Breaking Mechanism of Multiwalled Carbon Nanotubes Under Tensile Load, *Science*, 2000, **287**, 637–640.
- 41 J. V. Badding, High-Pressure Synthesis, Characterization, and Tuning of Solid State Materials, *Annu. Rev. Mater. Sci.*, 1998, **28**, 631–658.
- 42 B. R. Stanmore, J. F. Brillhac, and P. Gilot, The Oxidation of Soot: A Review of Experiments, Mechanisms and Models, *Carbon*, 2001, **39**, 2247–2268.
- 43 J. W. Long, M. Laskoski, T. M. Keller, K. A. Pettigrew, T. N. Zimmerman, S. B. Qadri, and G. W. Peterson, Selective-Combustion Purification of Bulk Carbonaceous Solids to Produce Graphitic Nanostructures, *Carbon*, 2010, **48**, 501–508.
- 44 J. Heyes, K. Anastakis, W. de Jong, A. van Hoesel, W. Roebroeks, and M. Soressi, Selection and Use of Manganese Dioxide by Neanderthals, *Sci. Rep.*, 2016, **6**, 22159.
- 45 M. G. Tucker, D. A. Keen, M. T. Dove, A. L. Goodwin, Q. Hui, RMCProfile: Reverse Monte Carlo for Polycrystalline Materials, *J. Phys. Condens. Matter*, 2007, **19**, 335218.
- 46 J.-Y. Luo, Y.-G. Wang, H.-M. Xiong, and Y.-Y. Xia, Ordered Mesoporous Spinel LiMn₂O₄ by a Soft-Chemical Process as a Cathode Material for Lithium-Ion Batteries, *Chem. Mater.*, 2007, **19**, 4791–4795.
- 47 S. Ching, J. L. Roark, N. Duan, and S. L. Suib, Sol–Gel Route to the Tunneled Manganese Oxide Cryptomelane, *Chem. Mater.*, 1997, **9**, 750–754.
- 48 J. W. Long, K. E. Swider-Lyons, R. M. Stroud, and D. R. Rolison, Design of Pore and Matter Architectures in Manganese Oxide Charge-Storage Materials, *Electrochem. Solid-State Lett.*, 2000, **3**, 453–456.
- 49 J. Luo, A. Huang, S.-H. Park, S. L. Suib, C.-L. O'Young, Crystallization of Sodium–Birnessite and Accompanied Phase Transformation, *Chem. Mater.*, 1998, **10**, 1561–1568.
- 50 C. A. Beasley, M. B. Sassin, and J. W. Long, Extending Electrochemical Quartz Crystal Microbalance Techniques to Macroscale Electrodes: Insights on Pseudocapacitance Mechanisms in MnO_x-Coated Carbon Nanofoams, *J. Electrochem. Soc.*, 2015, **152**, A5060–A5064.
- 51 S.-B. Ma, K.-W. Nam, W.-S. Yoon, X.-Q. Yang, K.-Y. Ahn, K.-H. Oh, and K.-B. Kim, Electrochemical Properties of Manganese Oxide Coated onto Carbon Nanotubes for Energy-Storage Applications, *J. Power Sources*, 2008, **178**, 483–489.
- 52 H. A. Laitinen and W. E. Harris, *Chemical Analysis*, 2 ed., McGraw-Hill, New York, 1975, p. 14.

-
- 53 P. Daum, J. R. Lenhard, D. R. Rolison, and R. W. Murray, Chemically Modified Electrodes. 21. Diffusional Charge Transport Through Ultrathin Films of Radio Frequency Plasma Polymerized Vinylferrocene at Low Temperature. *J. Am. Chem. Soc.*, 1980, **102**, 4649–4653.
- 54 M. M. Thackeray, Manganese Oxides for Lithium Batteries, *Prog. Solid State Chem.*, 1997, **25**, 1–71.